

# *Supporting Information For*

## Unusual Sonochemical Assembly between Carbon Allotropes for High Strain-Tolerant Conductive Nanocomposites

Zhaoliang Zheng,<sup>†,¶</sup> Jidong Jin,<sup>‡</sup> Jin-Chao Dong,<sup>§</sup> Bo Li,<sup>||</sup> Guang-Kui Xu,<sup>#</sup> Jian-Feng Li,<sup>§</sup> Dmitry G. Shchukin<sup>†\*</sup>

<sup>†</sup> Stephenson Institute for Renewable Energy and Department of Chemistry, University of Liverpool, Liverpool, L69 7ZD, United Kingdom.

Email: [d.shchukin@liverpool.ac.uk](mailto:d.shchukin@liverpool.ac.uk)

<sup>¶</sup> Present Address: Max Planck Institute for Polymer Research, Ackermannweg 10, 55128 Mainz, Germany.

<sup>‡</sup> Department of Chemistry, Chemistry Research Laboratory, University of Oxford, Oxford OX1 3TA, United Kingdom.

<sup>§</sup> MOE Key Laboratory of Spectrochemical Analysis and Instrumentation, State Key Laboratory of Physical Chemistry of Solid Surfaces, College of Chemistry and Chemical Engineering, Xiamen University, Xiamen 361005, China.

<sup>||</sup> Institute of Biomechanics and Medical Engineering, AML, Department of Engineering Mechanics, Tsinghua University, Beijing 100084, China.

<sup>#</sup> International Center for Applied Mechanics, State Key Laboratory for Strength and Vibration of Mechanical Structures, Xi'an Jiaotong University, Xi'an, 710049, China.

## SUPPORTING INFORMATION CONTENTS

### Part I. Supplementary Experimental Section

- Co-sonication
- Observations
- XPS analysis
- UV-vis analysis
- FTIR-KBr analysis
- DLS and zeta-potential analysis
- Numerical simulations

### Part 2. Supporting Information for research on roots-like covalent bonding

- Table S1. DLS size, zeta potential and morphology of samples
- Figure S1 UV-vis and corresponding Tauc plots of samples
- Figure S2 XPS wide scan spectra of SCNC-15, GO+CNT, p-GO and GO-15.
- Figure S3. TEM images of GO+CNT
- Figure S4. AFM and SEM images of GO+CNT and SCNC-15
- Figure S5. Optical image of oil-in-water droplets stabilized by SCNC-15
- Figure S6. TEM image of microcapsules made by GO+CNT or SCNC-15 as stabilizer

### Part 3. Supporting Information for differentiating SCNC-n, GO-n and GO+CNT

- Figure S7. Averaged Raman spectrum of p-GO, CNT, GO-15, GO+CNT and SCNC-15
- Figure S8. SEM images of Raman samples of SCNC-15 and GO+CNT
- Figure S9. Raman map of the intensity of ID/IG of p-GO, GO-15, SCNC-15, GO+CNT, CNT and SCNC-n
- Figure S10. KBr FTIR spectra of p-GO, Go-15, GO+CNT and SCNC-n
- Figure S11. UV-vis spectra of DPPH solutions for reference
- Figure S12. MALDI-TOF mass spectrum of SCNC-15 and GO-15 at 5k-50k Da
- Figure S13. Experiment setup for sonication and in-line detection of CO<sub>2</sub> produced
- Figure S14. SEM images of SCNC-1 and SCNC-5
- Figure S15. MALDI-TOF mass spectrum of a small molecular fragments of sonicated GO and fullerene, and physical mixture of GO and fullerene

- Figure S16.  $I_G$  versus  $\omega_G$  recorded on various spots on regions of physical mixture of GO and fullerene, sonicated GO and fullerene and sonicated GO and fullerene

- Figure S17. SEM images and Raman analysis of composites derived from co-sonication.

### Part 4. Supporting Information for strain-tolerant structural integrity and conductance

- Figure S18. SEM and AFM images of GO-15 and p-GO
- Figure S19.  $\omega_G$  and  $I_G$  as a function of strain for p-GO, GO-15, and GO+CNT.
- Figure S20. SEM images of p-GO and GO+CNT under the strain of 40%
- Figure S21. Summary of the G mode intensity of samples exposed to different strains
- Figure S22. AFM image of SCNC-15 dried on silicon substrate. Optical image of SCNC-15 loaded between two electrodes. I-V curves of p-GO and SCNC-15
- Figure S23. Raman map of D/G intensity ratio of SCNC-15 at strain of (a) 0 and (b) 160%
- Figure S24. Sharp contrast of relative resistance change between SCNC-15 and GO+CNT
- Table S2. Reported stretchable nano-carbonaceous materials
- References

## Part I. Supplementary Experimental Section

**Co-sonication.** Co-sonication of GO with other carbon-based materials follows the same sonication parameters in the Method section. To demonstrate the possible detrimental effect of collision, 0.32 and 0.16 ml of 2.5 mg/ml C60 dispersion in NMP were added before sonication, leading to the samples named 95%GO/5%C60 and 97.5%GO/2.5%C60. For other secondary materials, we weighted 0.8 mg of fullerene and ribbon powder and one carbon fibre (10 cm in length).

**Observations.** GO-CNT hybrids were investigated using a JEOL Transmission Electron Microscopy 2100FCs with a Schottky Field Emission Gun transmission electron microscope (200 kV accelerating voltage). Samples were collected on carbon-coated copper grids (Holey Carbon Film, 300 mesh Cu, Agar Scientific, Essex, UK). SEM analysis was performed using a JSM-7001F Scanning Electron Microscope from JEOL. The samples were coated with chromium for 30 s and examined. To get the free flake samples, the aqueous mixtures were cryogenically frozen by submersion in liquid N<sub>2</sub> before being freeze-dried in a Virtis AdVantage freeze drier (duration: 48 h, shelf temperature: -90 °C). To make supported samples, the dispersions were drop-casted and naturally dried on the quartz slides. The AFM images were collected via a Bruker Multimode 8 system. Image analysis was performed using nanoscale analysis software (Bruker). The samples were diluted to 0.1 mg/mL and then dropped on a clean silicon plate. The final loading and drying was conducted by a spin coater.

**XPS analysis.** The XPS data were recorded on a Kratos Axis Supra instrument (Kratos Analytical, Manchester, UK) using monochromatic Al K $\alpha$  radiation (1486.7 eV, 225 W). Survey scan spectra were acquired using a pass energy of 160 eV and a 1 eV step size. Narrow region

scans were acquired using a pass energy of 20 eV and a 0.1 eV step size. The hybrid lens mode was used in both cases. A charge neutralizer was used throughout as the samples were mounted such that they were electrically isolated from the sample bar. Several analysis points were analysed per sample. The spectra were calibrated to a binding energy of 285.0 eV for the hydrocarbon C 1s peak (sp<sup>3</sup> peak) post acquisition. The data were processed and analysed using the Kratos ESCApe software.

**UV-vis analysis.** For tracking the sonication process, the original concentrations of the mixtures were diluted with deionized water roughly to 100-500 times lower in order to assure  $\pi$ - $\pi^*$  peak below 2 a.u. The solutions were measured at an Evolution 201 UV-vis spectrophotometer. DPPH radical exhibits a deep violet colour in solution due to a strong absorption band, which becomes colorless or pale yellow when neutralized. This property allows visual monitoring of the existence of H-donator, and the number of initial radicals can be quantified based on the change in the optical absorption at 516 nm. The specific steps were as follows: First, an ethanol solution of DPPH was prepared at 0.1 mmol/L and stored at -20 °C in dark. Second, 5 mL of the reactant mixture was added to 3 mL of DPPH solution. The mixture was filtered after 30 min aging in dark. The absorbance at 516 nm of a control solution from 3 mL of DPPH mixed with 5 mL of p-GO solution and blank solution from 3 mL of DPPH mixed with 5 mL of sonicated water were also measured. The reference was made by mixing 5 mL of water and 3 mL of DPPH with certain concentrations.

**FTIR-KBr analysis.** The characterization of functional groups was conducted by Fourier-transform infrared spectroscopy using a TENSOR II (Bruker, Germany). The reactant mixture with roughly 1wt% solid weight of KBr powders were taken and mixed with KBr powder,

followed by dry under vacuum overnight. Absorbance measurements were taken from the pressed pellets with 128 scans from 400 to 4000  $\text{cm}^{-1}$ .

**DLS and zeta-potential analysis.** The flake characteristics, such as z-average diameter, polydispersity index (PDI) and zeta potential values were obtained by DLS using a Malvern Zetasizer ZS and disposable capillary cells (DTS1070, Malvern Instruments Inc). Three sub-runs per measurement were conducted at 25 °C and a backscattering angle of 173°. The samples for the size and electrophoretic mobility have concentration of 0.25 mg/mL. The obtained size data were further analyzed by the CONTIN model. The zeta-potential was measured using the Smoluchowski method and an auto mode. The manuscript should start with a brief introduction that lays out the problem addressed by the research and describes the paper's importance. The scientific question being investigated should be described in detail. The introduction should provide sufficient background information to make the article understandable to readers in other disciplines and provide enough context to ensure that the implications of the experimental findings are clear.

**Numerical simulations.** Our complementary simulations reveal the randomly in-plane compressive/stretching strains provided by anchoring CNTs on SCNC-15 give rise to the out-of-plane buckling. SCNC-15 behaves as a thin sheet resting on an elastic compliant substrate during the stretching process, which can be modelled by the Föppl–von Kármán plate.<sup>[1]</sup> We introduce pre-strains to mimic this expansion in simulations, and our results show that anisotropic expansion will induce labyrinthine crumpling of SCNC-15. Uniaxial stretching can relax compressive strain, leading to a non-equibiaxial stress field in SCNC-15, which tends to align the crumples along the stretching direction. More relaxation of compressive strain by increasing uniaxial stretching can give rise to a groove pattern. To gain mechanical insight into the

crumpling of graphene layer, we model the graphene layer as a thin elastic plate, which is bonded to a compliant substrate. Both the thin plate and the substrate are assumed to be isotropic and linear. We use the Föppl–von Kármán elastic nonlinear plate theory to model the thin plate. The strains of the plate are written as

$$\varepsilon_{\alpha\beta} = \varepsilon_{\alpha\beta}^{\text{pre}} + \frac{1}{2}(u_{\alpha,\beta} + u_{\beta,\alpha}) + \frac{1}{2}w_{,\alpha}w_{,\beta} \quad (\alpha, \beta=1,2), \quad (1)$$

where  $\varepsilon_{\alpha\beta}^{\text{pre}}$  denote the pre-strains introduced in the experiments,  $u_\alpha$  and  $w$  represent the in-plane and normal displacements of the plate, respectively. In the case of infinitesimal stains, the Hooke's law for the plate reads

$$\sigma_{\alpha\beta} = \bar{E}_f \left[ (1 - \nu_f) \varepsilon_{\alpha\beta} + \nu_f \varepsilon_{\gamma\gamma} \delta_{\alpha\beta} \right], \quad (2)$$

where  $\sigma_{\alpha\beta}$  and  $\varepsilon_{\alpha\beta}$  are stresses and strains, respectively;  $\bar{E}_f = E_f / (1 - \nu_f^2)$  with  $E_f$  and  $\nu_f$  being Young's modulus and Poisson's ratio of the plate, respectively;  $\delta_{\alpha\beta}$  denotes the Kronecker delta. The repeated Greek subscript implies summation over 1 and 2. The mechanical equilibrium of the thin plate obeys

$$\begin{aligned} \sigma_{\alpha\beta,\beta} &= T_\alpha / h, \\ T_3 &= -\frac{h^3 \bar{E}_f}{12} \nabla^4 w + (h \sigma_{\alpha\beta} w_{,\alpha})_{,\beta}, \end{aligned} \quad (3)$$

where  $h$  denotes the thickness of the plate;  $T_1$  and  $T_2$  are the interfacial shear stress and  $T_3$  is the interfacial normal stress at the interface between the thin plate and the substrate.

The elastic response of the compliant substrate is governed by

$$\sigma_{ij,j} = 0 \quad (i, j=1,2,3), \quad (4)$$

and the linear constitutive law of the substrate reads

$$\sigma_{ij} = \frac{E_s}{1+\nu_s} \varepsilon_{ij} + \frac{\nu_s E_s}{(1+\nu_s)(1-2\nu_s)} \varepsilon_{kk} \delta_{ij}, \quad (5)$$

where  $E_s$  and  $\nu_s$  are Young's modulus and Poisson's ratio of the substrate, respectively. Latin subscripts  $i, j$ , and  $k$  take values 1, 2, and 3.  $\varepsilon_{ij}$  are strains, which are related to displacements  $u_i$  through

$$\varepsilon_{ij} = \frac{1}{2}(u_{i,j} + u_{j,i}). \quad (6)$$

We use the Fourier spectral method to solve the differential system provided above. This method allows us to capture the postbuckling behavior of the thin plate. The standard 2D Fourier transformation of function  $w(x_1, x_2)$  is

$$F[w(x_1, x_2)] = \hat{w}(k_1, k_2) = \int_{-\infty}^{\infty} \int_{-\infty}^{\infty} w(x_1, x_2) e^{-ik_1 x_1 - ik_2 x_2} dx_1 dx_2, \quad (7)$$

where the upper hat denotes the physical quantity in the Fourier space,  $k_1$  and  $k_2$  are the coordinates in the Fourier space. The relation of the interface stresses  $T_1$  and the displacements  $u_i$  in the Fourier space can be obtained as

$$\hat{T}_i = D_{ij} \hat{u}_j, \quad (8)$$

where the stiffness matrix  $D_{ij}$  of the substrate is derived as

$$[D_{ij}] = \frac{E_s}{(1+\nu_s)(6-8\nu_s)} \begin{bmatrix} \frac{4k^2(1-\nu_s)-k_2^2}{k} & \frac{k_1 k_2}{k} & 2ik_1(1-2\nu_s) \\ \frac{k_1 k_2}{k} & \frac{4k^2(1-\nu_s)-k_1^2}{k} & 2ik_2(1-2\nu_s) \\ -2ik_1(1-2\nu_s) & -2ik_2(1-2\nu_s) & 4k(1-\nu_s) \end{bmatrix}, \quad (9)$$

where  $k = \sqrt{k_1^2 + k_2^2}$ .

Substituting Eqs. (1) and (2) to (3) in the Fourier space, and combining Eq. (9), we can obtain the linear algebraic equations for  $\hat{u}_1$  and  $\hat{u}_2$

$$\begin{cases} \left( \hat{E}_f k_1^2 + \frac{1}{2} \hat{E}_f (1 - \nu_f) k_2^2 + \frac{D_{11}}{h} \right) \hat{u}_1 + \left[ \frac{1}{2} \hat{E}_f (1 + \nu_f) k_1 k_2 + \frac{D_{12}}{h} \right] \hat{u}_2 = \hat{b}_1 \\ \left[ \frac{1}{2} \hat{E}_f (1 + \nu_f) k_1 k_2 + \frac{D_{12}}{h} \right] \hat{u}_1 + \left( \hat{E}_f k_2^2 + \frac{1}{2} \hat{E}_f (1 - \nu_f) k_1^2 + \frac{D_{22}}{h} \right) \hat{u}_2 = \hat{b}_2 \end{cases} \quad (10)$$

where

$$\begin{aligned} \hat{b}_1 &= -\frac{D_{13}}{h} \hat{w} + \frac{ik_1}{2} \hat{E}_f \left[ F \left[ (w_{,1})^2 \right] + \nu_f F \left[ (w_{,2})^2 \right] \right] \\ &\quad + \frac{ik_2}{2} \hat{E}_f (1 - \nu_f) F \left[ w_{,1} w_{,2} \right] + \bar{E}_f \left[ F \left[ \varepsilon_{11,1}^{\text{pre}} \right] + \nu_f F \left[ \varepsilon_{22,1}^{\text{pre}} \right] \right], \\ \hat{b}_2 &= -\frac{D_{23}}{h} \hat{w} + \frac{ik_2}{2} \hat{E}_f \left[ F \left[ (w_{,2})^2 \right] + \nu_f F \left[ (w_{,1})^2 \right] \right] \\ &\quad + \frac{ik_1}{2} \hat{E}_f (1 - \nu_f) F \left[ w_{,1} w_{,2} \right] + \hat{E}_f \left[ F \left[ \varepsilon_{11,2}^{\text{pre}} \right] + \nu_f F \left[ \varepsilon_{22,2}^{\text{pre}} \right] \right]. \end{aligned}$$

The normal equilibrium equation in terms of  $\hat{w}$  is derived as

$$\left( D_{33} + \frac{h^3 \hat{E}_f}{12} k^4 \right) \hat{w} = ik_\beta F \left[ h \sigma_{\alpha\beta} w_{,\alpha} \right] - D_{3a} \hat{u}_a. \quad (11)$$

We introduce a numerical viscosity term  $\varsigma \hat{w}$  to Eq. (11) and obtain the iterative algorithm

$$\hat{w}^{(n+1)} = \left( \varsigma + D_{33} + \frac{h^3 \hat{E}_f}{12} k^4 \right)^{-1} \left\{ \varsigma \hat{w}^{(n)} + ik_\beta F \left[ h \sigma_{\alpha\beta} w_{,\alpha}^{(n)} \right] - D_{3a} \hat{u}_a^{(n)} \right\}, \quad (12)$$

where the superscript (n) represents a physical quantity in the  $n$ -th iterative step. A small random displacement perturbation is prescribed to trigger the wrinkling. When the total potential energy in the system converges to a constant, we will stop the iteration.

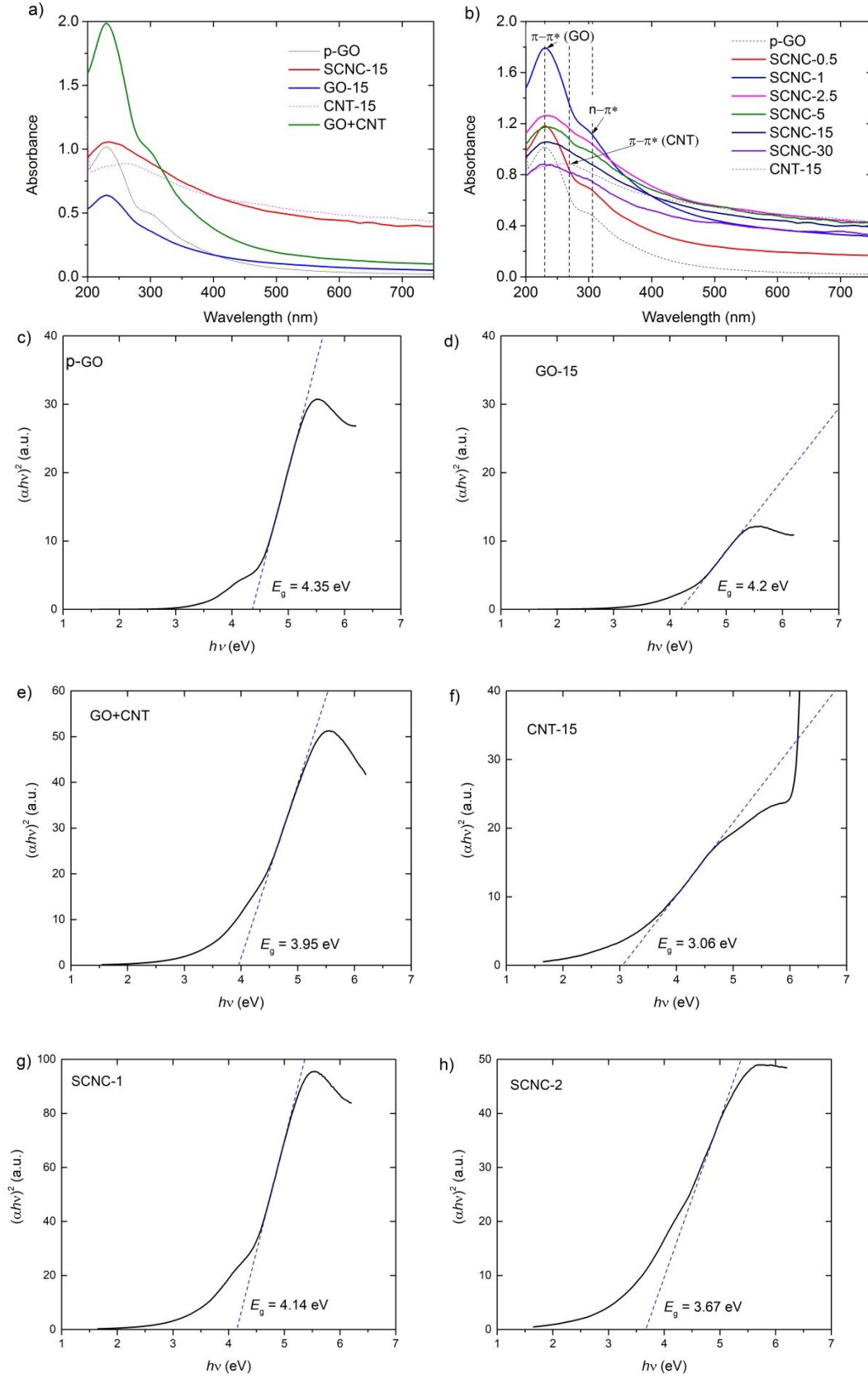


**Part 2. Supporting Information for research on roots-like covalent bonding.**

**Table S1.** DLS size, zeta potential and morphology of samples

	Zeta-size (nm)	Zeta-potential (mV)	Morphology <sup>[b]</sup>
p-GO	1628	-12.6	Sheets
SCNC-1	3158 <sup>[a]</sup>	-10.1	Sheets
SCNC-5	2850 <sup>[a]</sup>	-9.88	Sheets
SCNC-15	932.4	-8.79	Sheets
SCNC-30	856.3	-8.97	Sheets
GO-1	730.6	-6.12	Sheets
GO-5	588.7	-5.66	Sheets
GO-15	491.1	-12.4	Sheets
GO 0°C without Argon sonicated 15 min	3462 <sup>[a]</sup>	-21.8	Spheres

[a] The value beyond the reliability limit of DLS. [b] After lyophilisation.



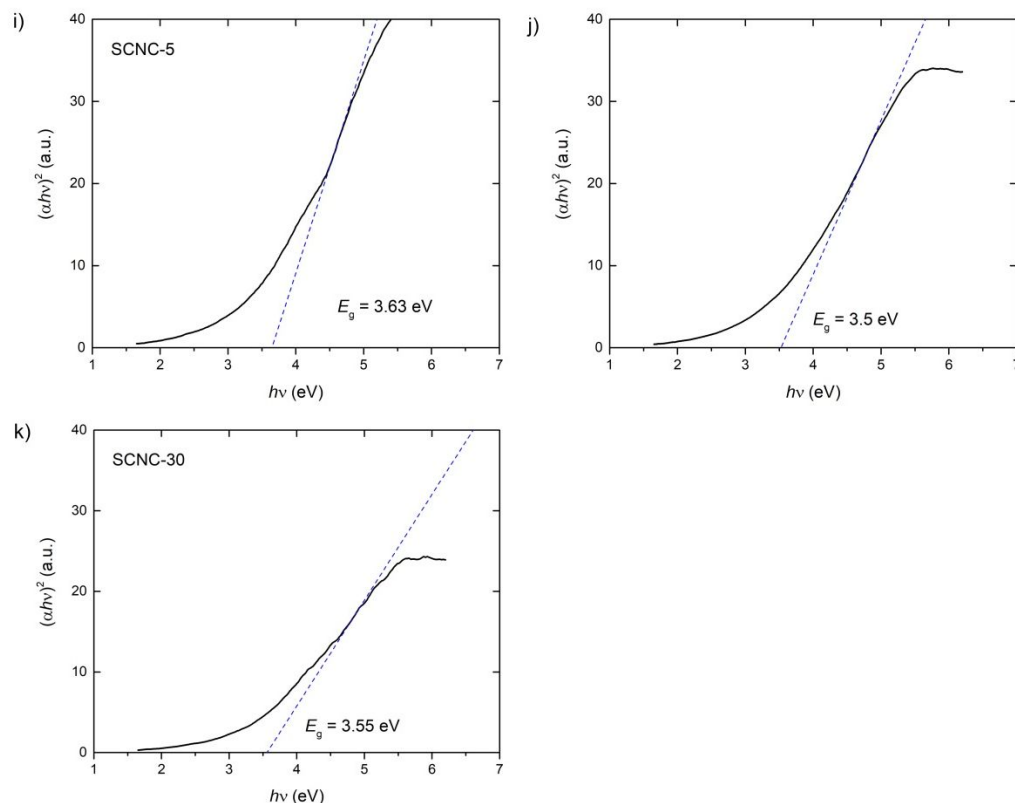


**Figure S1** (a-b) UV-vis spectra of samples. (c-k) Corresponding Tauc plots of them.

UV-Vis absorption spectra were obtained from aqueous dispersions of reaction mixture at different sonication time in a quartz cuvette. The absorption peak at 230 nm has been assigned to the  $\pi$ - $\pi^*$  transition of the C=C bonds of GO. The typical absorption band at 270 nm is attributed to a  $\pi$ - $\pi^*$  transition characteristic of CNTs.<sup>2</sup> A small shoulder near 300 nm was observed in all GO samples, which is attributed to the  $n \rightarrow \pi^*$  transition of C=O. SCNC-0.5 and 1 show the similar spectra to GO because entangled CNTs are hardly active in the wavelength region between 200 and 800 nm. The absorption peaks at 230 and 270 nm are coupled into a wider one for the sample of SCNC-5, indicating an assembly of GO and CNTs. By comparing the absorbance at 230-270 nm at the spectrum of GO-15, the peak at 260 nm of SCNC-15 is attributed to the blue shift of  $\pi$ - $\pi^*$  transition of CNTs. We believe it implies the formation of covalent bonds between GO and CNTs. The  $\pi$ - $\pi^*$  transition of the C=C bonds of GO blue shifted

slightly for the sample of SCNC-30, which is due to the decrease of  $sp^2$  regions induced by further fragmentation. Furthermore, GO+CNT is analogous to p-GO but dramatically different to SCNC-15. The band gap energy of samples were determined by using a Tauc plot with a linear extrapolation.<sup>3</sup>

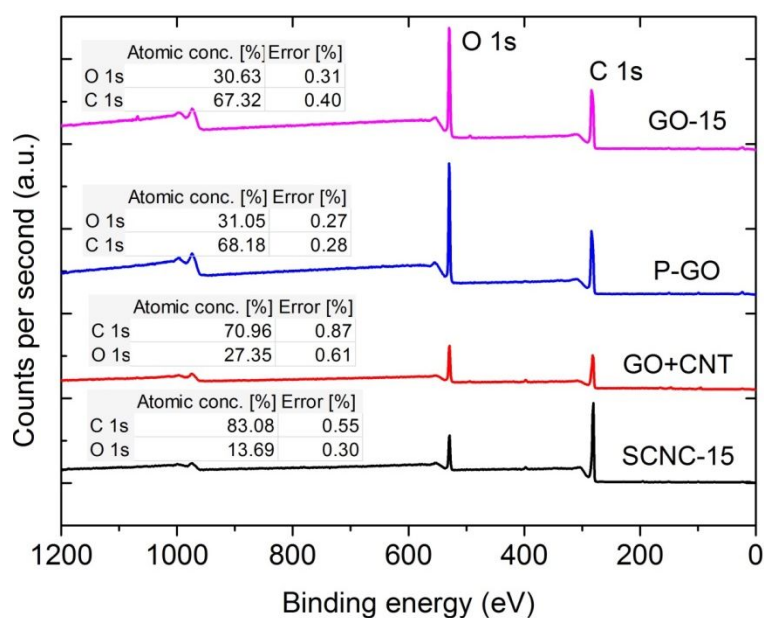


**Figure S2.** XPS wide scan spectra of SCNC-15, GO+CNT, p-GO and GO-15. The corresponding atomic concentrations of carbon and oxygen are shown as well.

**Description of experimental details on how to distinguish between robustness of C-C covalent bonds and  $\pi$ - $\pi$  conjugation:** First, less than 10% of the nanotubes at GO+CNT show the open ends (Figure S3). Second, the deprotonation of  $\text{-COOH}$  groups at the neutral pH offset the effect of  $\pi$ - $\pi$  attraction and led to detachment of oxidized CNTs from GO+CNT, whereas SCNC-15 remained unaffected (Figure S4). Third, the GO-CNT junctions were further exposed by spreading and trapping SCNC-15 laterally at the high-energy oil/water interfaces of the emulsion. It is because the further  $\pi$ - $\pi$  stacking of extra 2D flakes is suppressed by an increase in aggregate bending energy.<sup>4</sup> The nanotubes rooted firmly at the basal plane of GO shell in the presence of shearing forces during emulsification and conjugative affinity from the aromatic (toluene) oil phase. The toluene/water o/w emulsions were prepared using the mixture of toluene (1 mL) and the freshly made GO+CNT or SCNC-15 (~5 mL). The emulsification procedure is described as follows: the oil phase (toluene) and aqueous dispersion were added into a 20 mL glass vial, followed by pulse-sonication (10 s on, 5 s off) with an amplitude at 30% for 15 min. During sonication, the vial was immersed in an ice bath to avoid overheating. The emulsion was obtained as Figure S5. The configurations of **I**, **II** and **III** are almost intact. However, Van der Waals attractions in GO+CNT are vulnerable, only leading to naked GO shells and reaggregation of detached MWCNTs (Figure S6). Taken together, GO-CNT junctions of SCNC-15 are much stronger than  $\pi$ - $\pi$  stacking interactions, which assure that **I**, **II** and **III** are characteristic evidence for the covalent bonds.

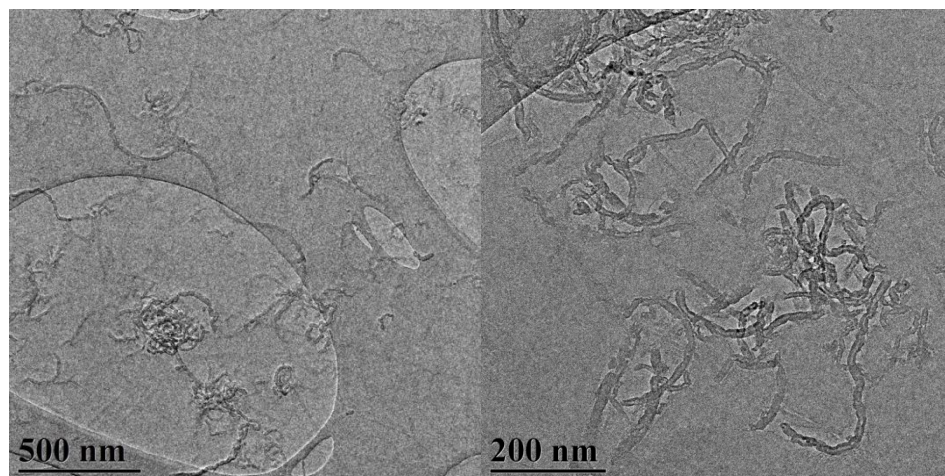


**Figure S3.** TEM images of GO+CNT.

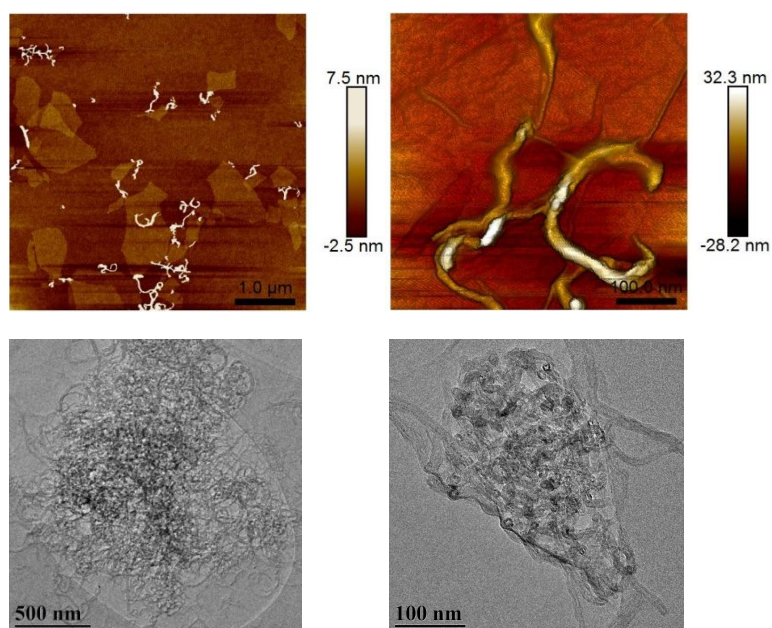


**Figure S4.** AFM images of GO+CNT (up left) and SCNC-15 (up right). SEM images of detached large CNT entanglement from GO+CNT (down left) and attached smaller CNT entanglement at SCNC-15 (down right).



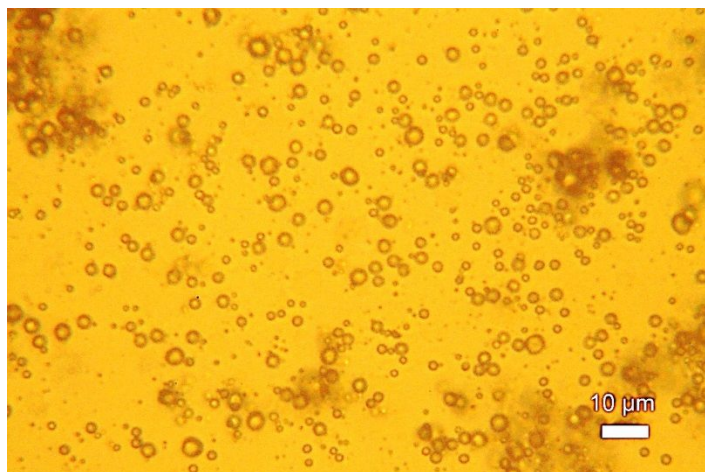


**Figure S5.** Optical image of oil-in-water droplets stabilized by SCNC-15.

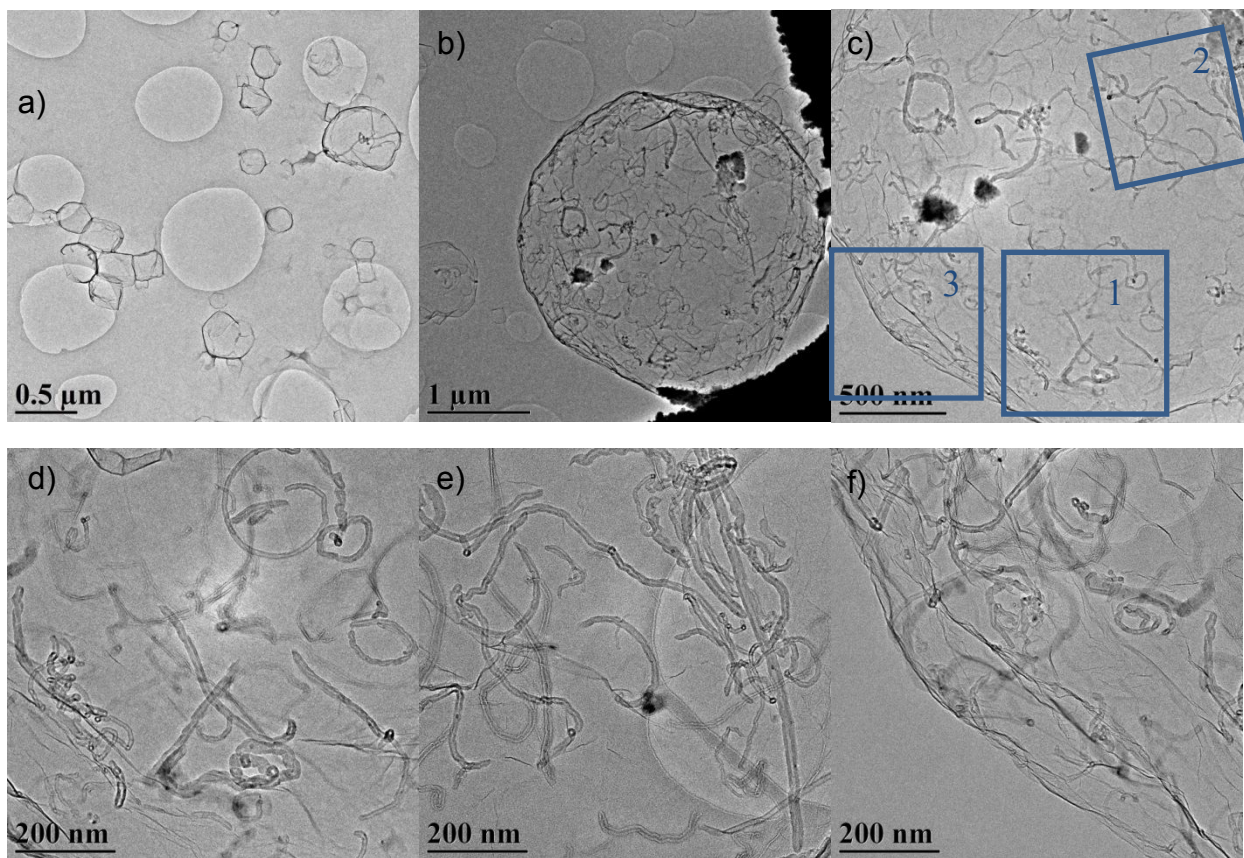


**Figure S6.** TEM image of microcapsules made by emulsification with GO+CNT (a) or SCNC-15 (b) as stabilizer. Three configurations of open-ended CNTs have been retained after emulsification, as shown in magnified zone of 1 (d), 2 (e) and 3 (f) of c.

### Part 3. Supporting Information for differentiating SCNC-n, GO-n and GO+CNT.

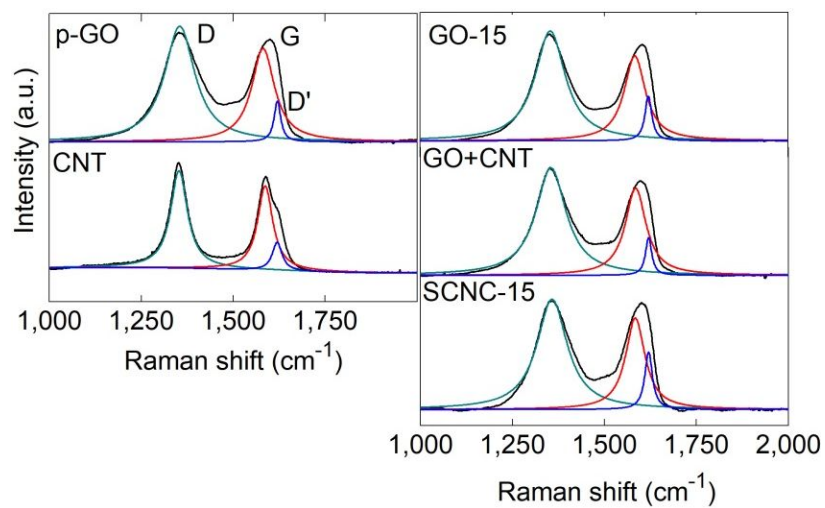


**Figure S7.** Averaged Raman spectrum is taken from 25×25 points of p-GO, CNT, GO-15, GO+CNT and SCNC-15. First-order Raman spectrum consists of three peaks: D ( $\sim 1350\text{ cm}^{-1}$ ) and D'-bands ( $\sim 1620\text{ cm}^{-1}$ ) are associated with defects at the edges or in the  $\text{sp}^2$  network; G band ( $\sim 1583\text{ cm}^{-1}$ ) is due to the bond stretching of planar C–C species, usually indicative of the degree of  $\text{sp}^2$  atomic arrangement. Fitting only with G and D band got the similar MAD trend. 2D-line cannot be used in this work due to its broadened and weak appearance.

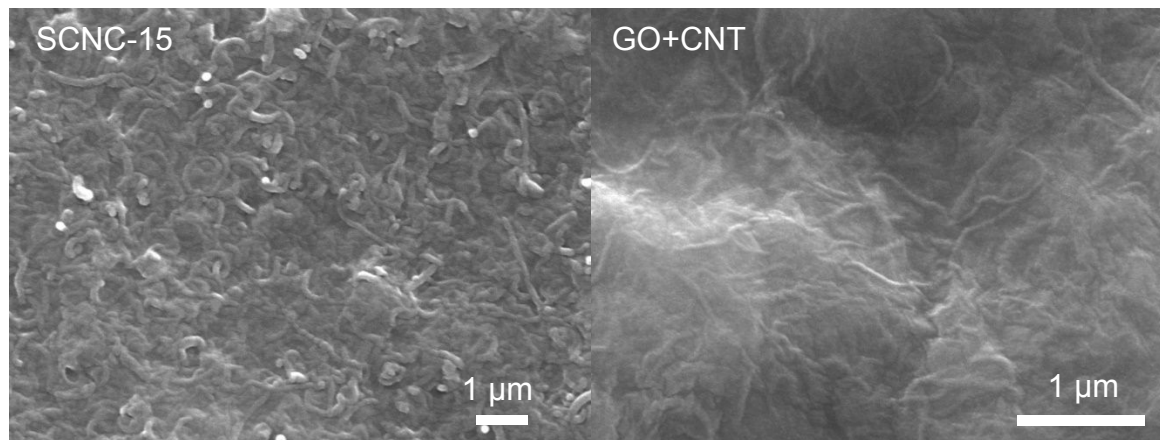


**Figure S8.** SEM images of Raman samples of SCNC-15 and GO+CNT.



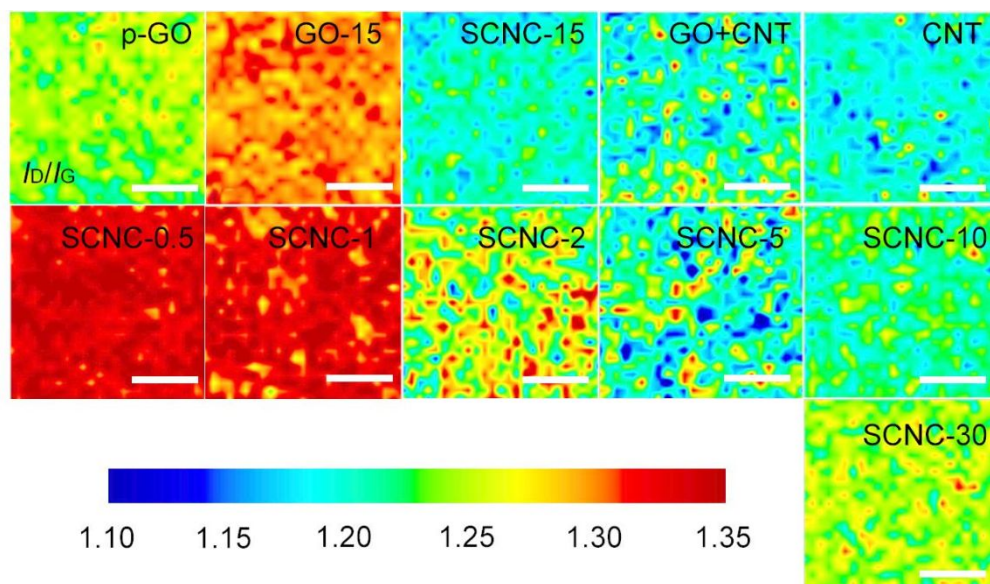


**Figure S9.** Raman map of the intensity of  $I_D/I_G$  of p-GO, GO-15, SCNC-15, GO+CNT, CNT and SCNC-0.5, 1, 2, 5, 10, and 30. Scale bar: 10  $\mu\text{m}$ .

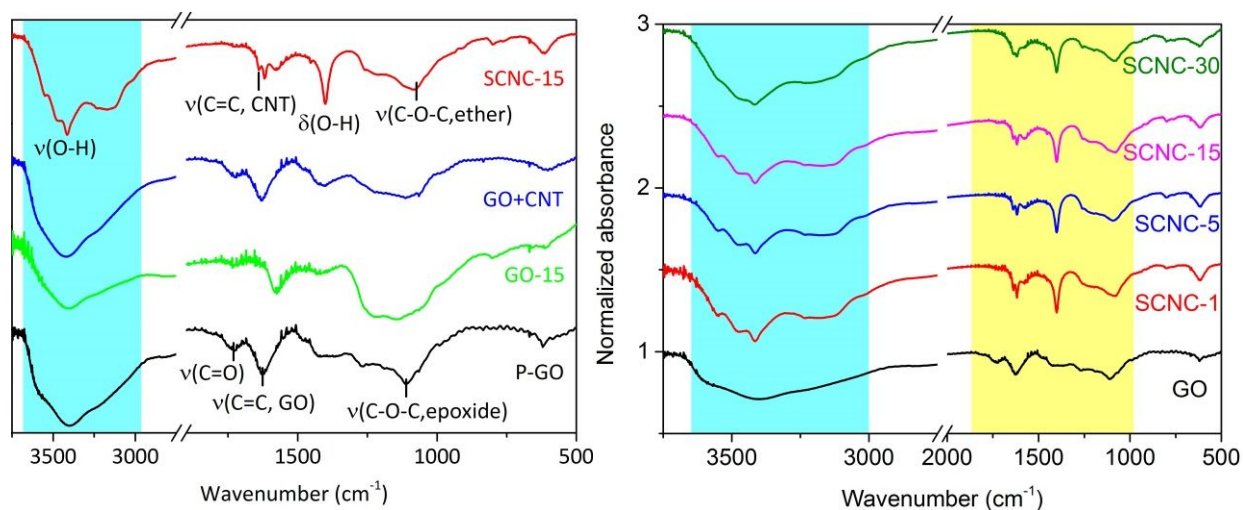


**Figure S10.** KBr FTIR spectra of p-GO, Go-15, GO+CNT and SCNC-n.

We monitored the evolution of oxygen species using Fourier transform infrared (FTIR) spectroscopy. As compared with p-GO, GO-15 and GO+CNT, the FTIR spectrum of SCNC-15 clearly shows the stronger and clearer O-H vibrational absorbance at 3250-3600 ( $\nu$  O-H) and

1400  $\text{cm}^{-1}$  as well as the vanish of carboxyl group (1730  $\text{cm}^{-1}$ ) at the edges. Surprisingly, the –OH group appears as early as the first minute of sonication, and so does the CNT characteristic graphitic domains (1640  $\text{cm}^{-1}$ ). Meanwhile, the band at 1109  $\text{cm}^{-1}$  linked to epoxide (C-O-C) groups<sup>5</sup> vanishes whereas the neighbouring (1060  $\text{cm}^{-1}$ ) for ether/alkoxy<sup>6</sup> species becomes dominant. Importantly, such spectral evolution cannot be seen in the scenarios without CNTs (GO-15) or ultrasonication (GO+CNT).

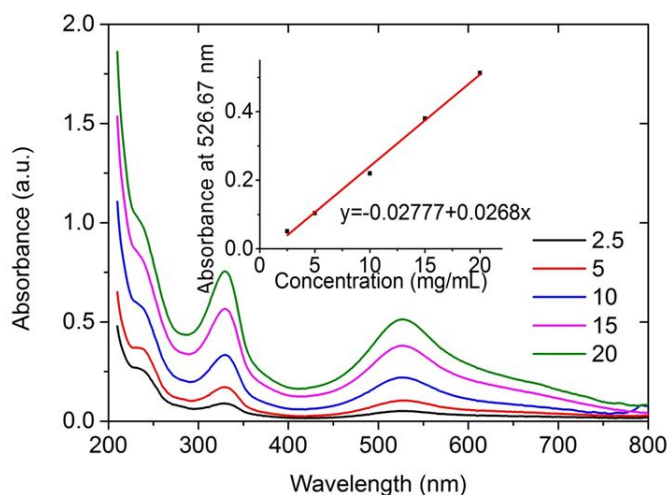


**Figure S11.** UV-vis spectra of DPPH solutions for reference.

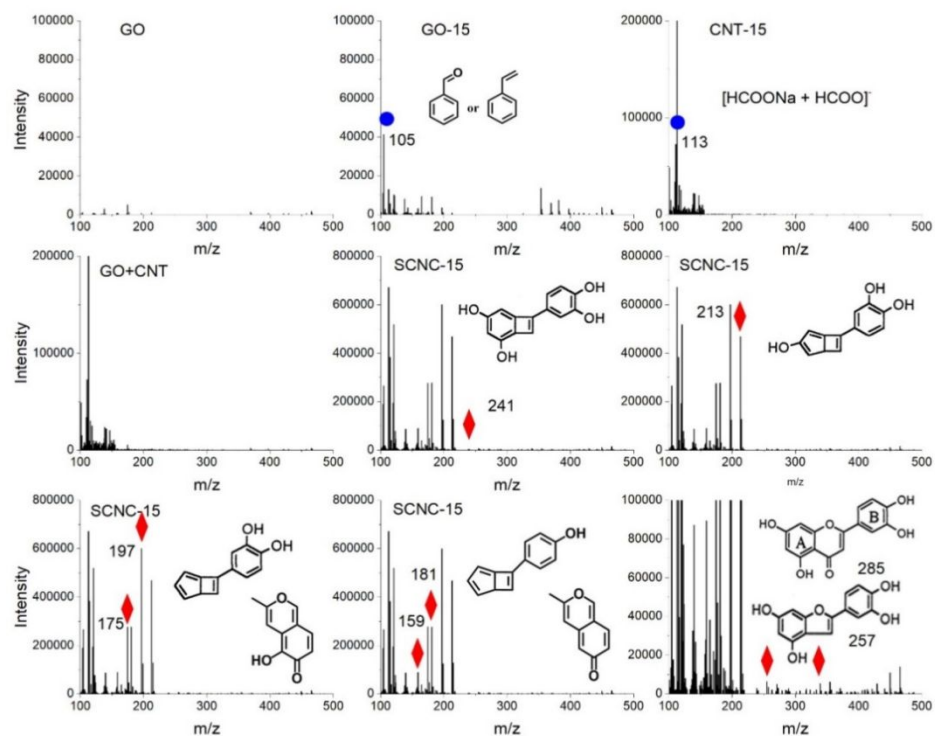
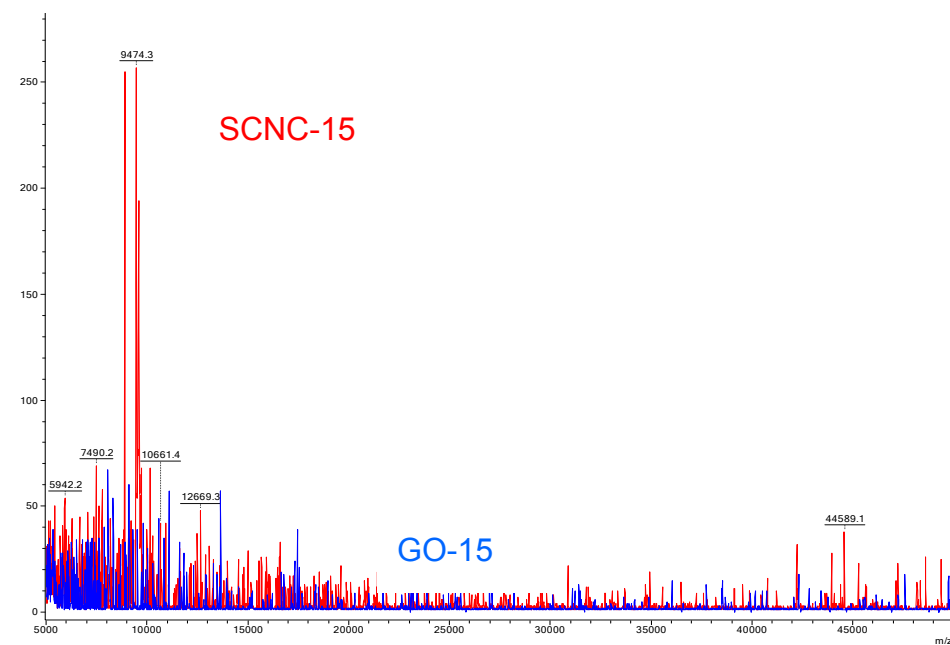


**Figure S12.** MALDI-TOF mass spectrum of SCNC-15 and GO-15 at 5k-50k Da. Proposed fragments at 0-4k Da are also demonstrated. ● Background signal. ♦ Fragments of flavonoid-type molecules.

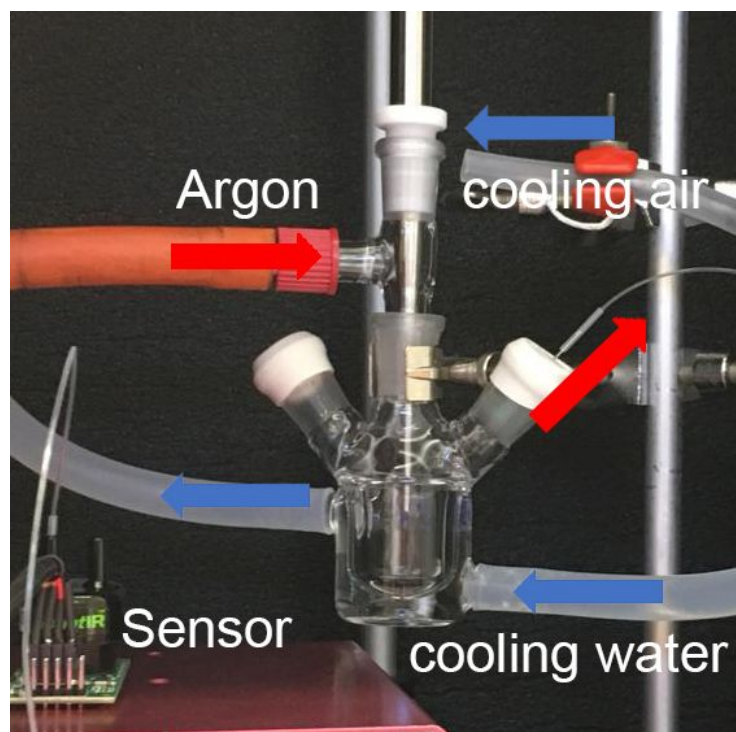


**Figure S13.** Experiment setup for SCNC-n and GO-n, and in-line detection of CO<sub>2</sub> produced during the sonication.

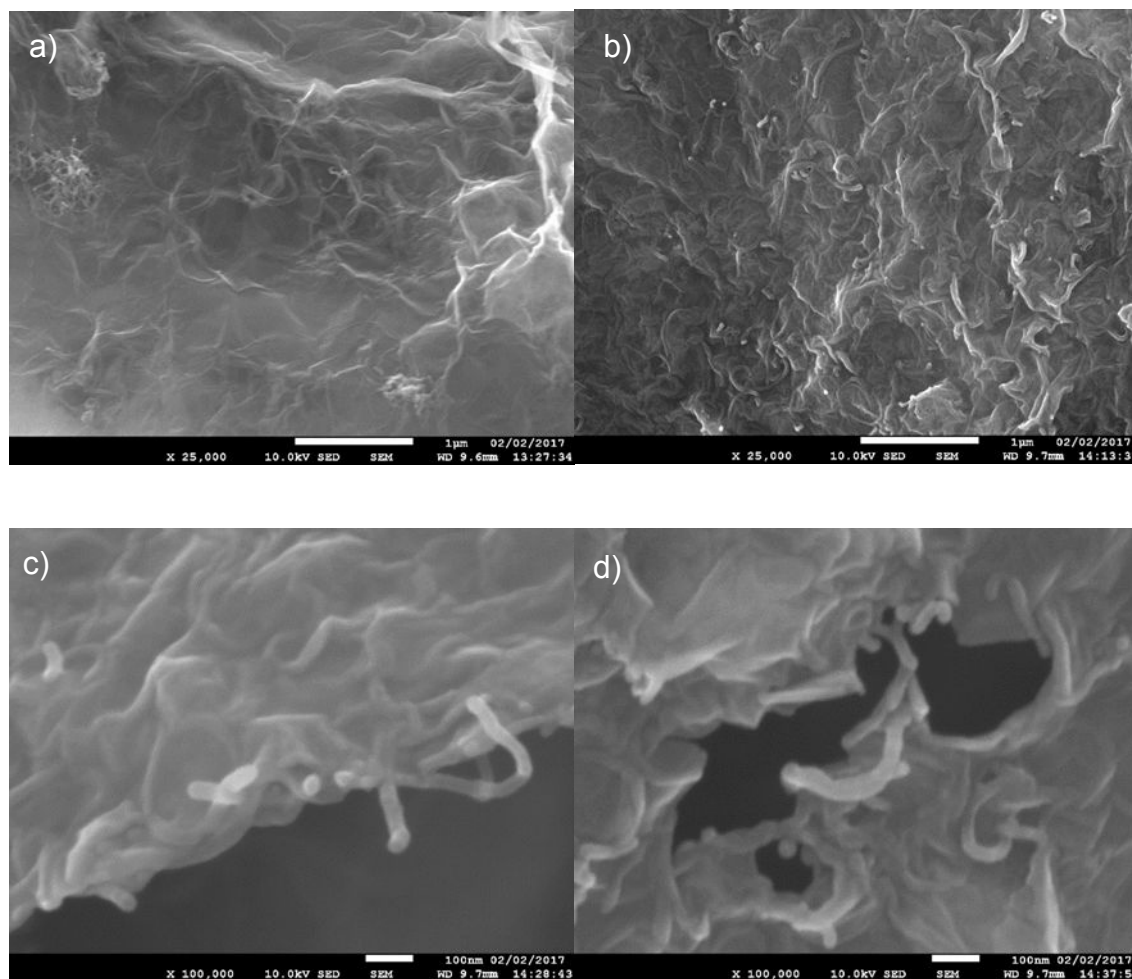


**Figure S14.** SEM images of (a) SCNC-1 and (b-d) SCNC-5

The SEM images of edge- and basal-plane of SCNC-1 and -5 elucidate how CNT help to ease the fragmentation of GO sheets. After 1 min, large CNT clusters can still be seen, meanwhile, CNT is seldom found at the edge. In contrast, the basal-planes of SCNC-5 are almost fully covered by CNT, which is comparable to SCNC-15. The edges, even notably, are adhered by a number of CNTs. During sonication, cavitation shatters the large sheets (p-GO) creating cracks that propagate from their edges to form fragments.<sup>7</sup> We conceive that the anchored CNT can on one hand relieve the cavitation applied at the GO surface and on the other hand cease the propagation of cracks at the edge.

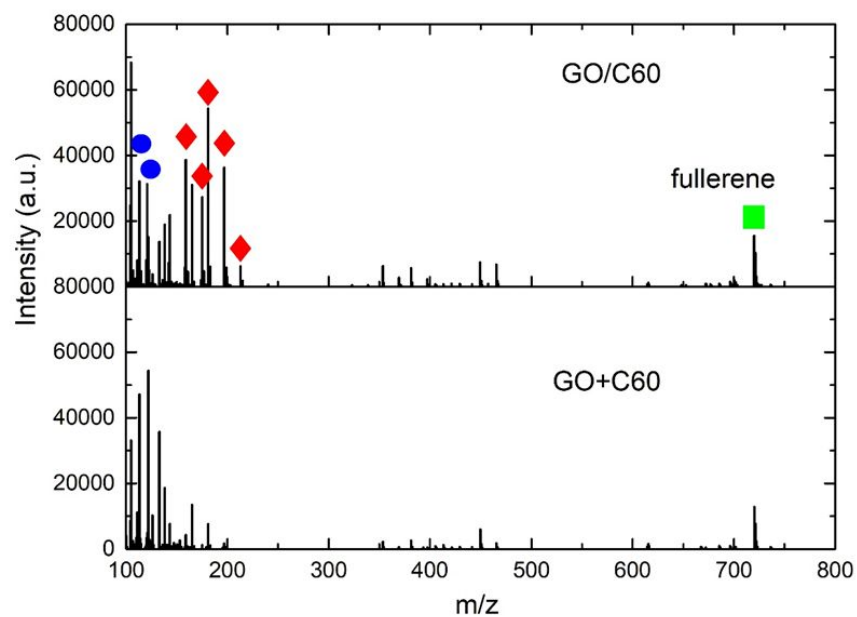


**Figure S15.** MALDI-TOF mass spectrum of a small molecular fragments of sonicated GO and fullerene, and physical mixture of GO and fullerene. Besides the small-molecular fragments reported ones from flavonoid. Fullerene can also be detected. ● Background signal. ♦ Fragments of flavonoid-type molecules.



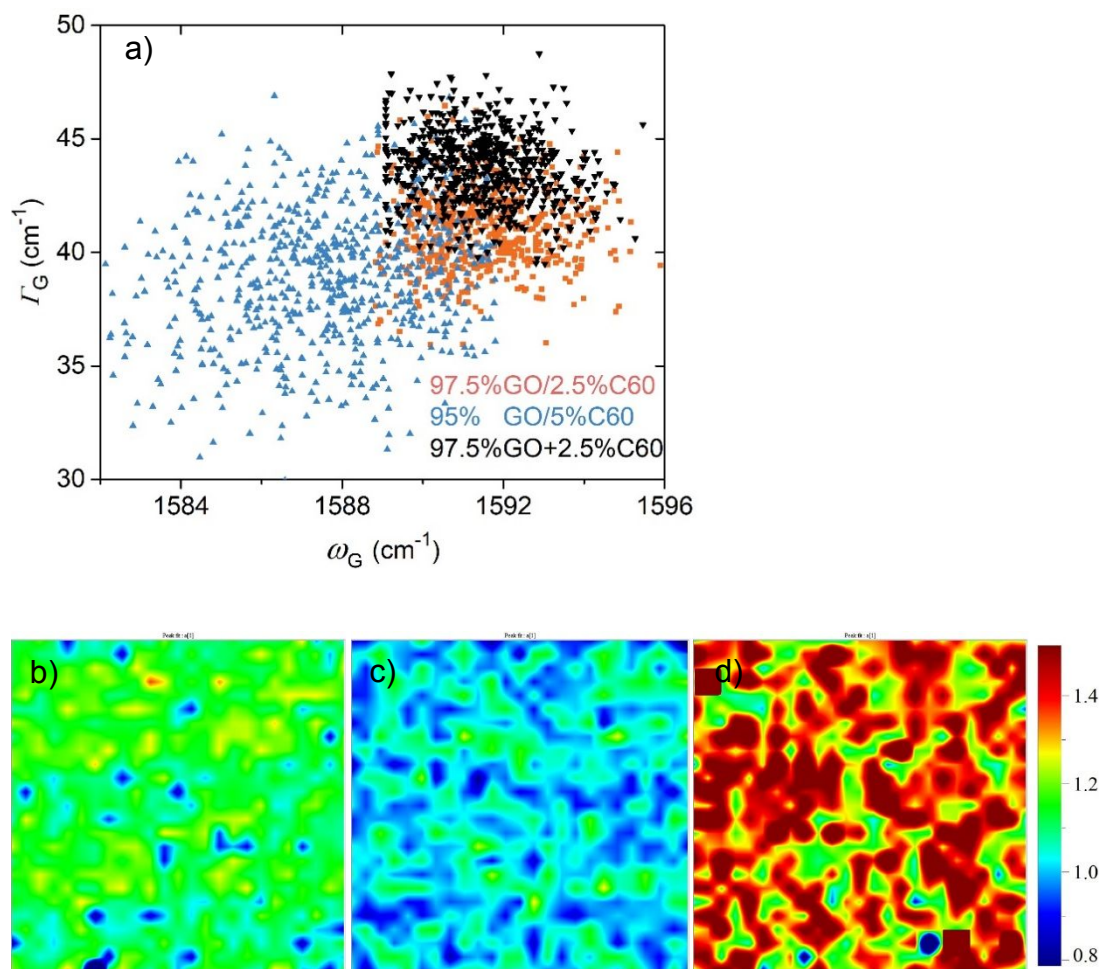


**Figure S16.** (a)  $I_G$  versus  $\omega_G$  recorded on various spots on regions of physical mixture of GO and fullerene (97.5 and 2.5 wt%, 97.5%GO+2.5%C60, black), sonicated GO and fullerene (97.5 and 2.5 wt%, 97.5%GO/2.5%C60 orange) and sonicated GO and fullerene (95 and 5 wt%, 95%GO/5%C60, blue). Raman map of the intensity of  $I_D/I_G$  of (b), 97.5%GO+2.5%C60, (c) 97.5%GO/2.5%C60 and (d) 95%GO/5%C60. Scanning area  $25 \times 25 \mu\text{m}^2$ .

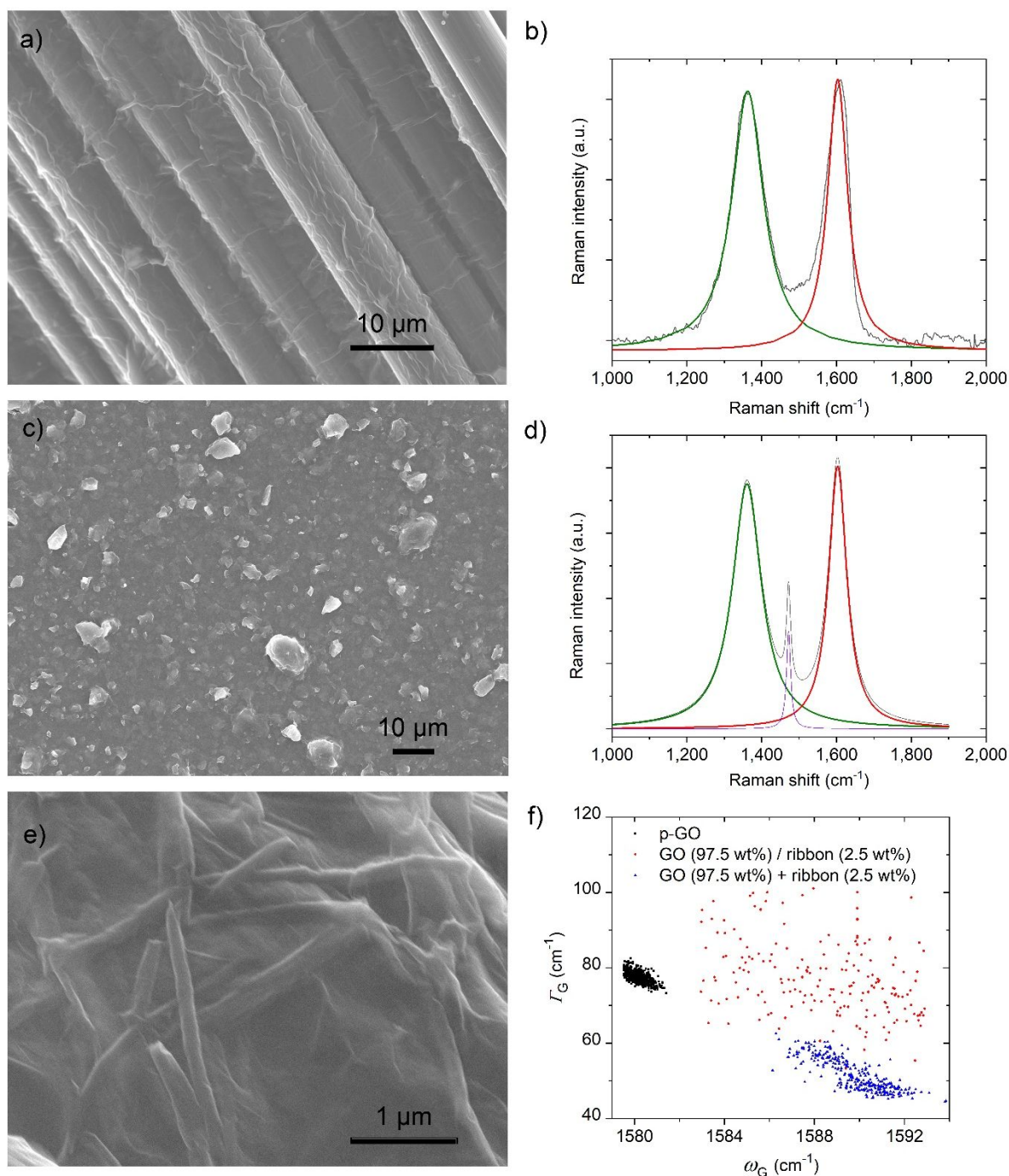


**Figure S17.** SEM images of composites derived from co-sonication of GO and a) carbon fibre, c) Fullerite and e) graphene nanoribbons. Raman spectrum of composites derived from co-sonication of GO and b) carbon fibre and d) Fullerite. f)  $I_G$  versus  $\omega_G$  recorded on spots on



regions of p-GO (black), physical mixture of GO and ribbon (97.5wt%GO+2.5wt%ribbon, blue) and sonicated GO and ribbon (97.5wt%GO/2.5wt%C60, red).

The secondary carbon-based materials in the binary-components system with different dimensions and size were further investigated. For example, carbon fibre with a diameter of 10  $\mu\text{m}$ , which were co-sonicated with p-GO. The sonication can shorten the length but remain the cross-section of carbon fibre intact. The fibres here can only be treated as 3D or quasi-2D objects, as the surface of carbon fibre was almost covered by GO. The corresponding  $I_D/I_G$  equals 1.48 (Figure S17a,b). Similarly, co-sonication with the aggregates of C60, namely Fullerite, can only led a high  $I_D/I_G$  value to 1.49 (Figure S17c,d). While, we know the pre-dispersion of C60 in NMP before co-sonication helped decrease  $I_D/I_G$  value to 1.18 (Figure S16). The Fullerites are only a large 3D objects to GO sheets. The final size after 15 min sonication is still 1-10  $\mu\text{m}$ . The  $I_D/I_G$  of the above composites are much higher than the SCNC-15 or even GO-15. We believe that the size of the secondary particles determines the effect of collisions. Interparticle velocities must depend on particle size. Sufficiently large particles will be only minimally accelerated by the cavitation shock waves.<sup>8</sup> Interparticle collisions still occur and surface morphology and chemical reactivity of GO can be affected, but the burst of fragmentation in our manuscript will not occur. Besides the size, the dimension could also matter. We co-sonicated 2D graphene nanoribbon with p-GO. The ribbons with similar length with CNT were rolled up into tubes and attached firmly on the uneven surface of GO (Figure S17e). The resulting  $I_D/I_G$  value is 1.13, much lower than those of p-GO (1.20), ribbons (1.92) and even slightly lower than the physical mixture of GO and nanoribbons (1.15). The explanation could be the  $\pi$ - $\pi$  conjugation between two 2D objects may play a dominant role to

sonication-assisted assembly; meanwhile, fragments contributes to the decrease of  $I_D/I_G$  as well. The MAD of GO/ribbon is 6.23. GO+ribbon, alike CO+CNT, has a MAD of 1.62 (Figure S17f).

#### Part 4. Supporting Information for strain-tolerant structural integrity and conductance

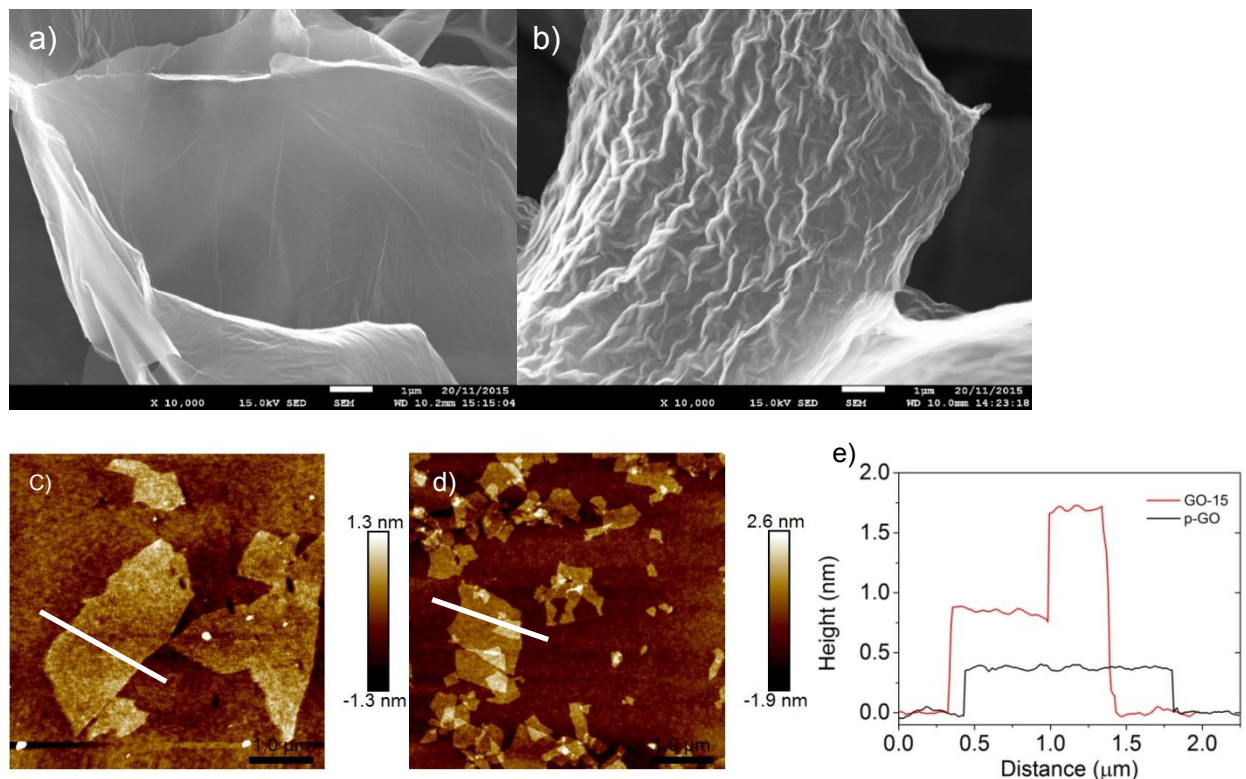


**Figure S18.** SEM images show the ripples or crumples of free-standing GO-15 a) and b) p-GO. AFM images unveil the flattened c) GO-15, d) p-GO and e) corresponding height measurement. Image of monolayer SCNC-15 is also shown in Figure S4.

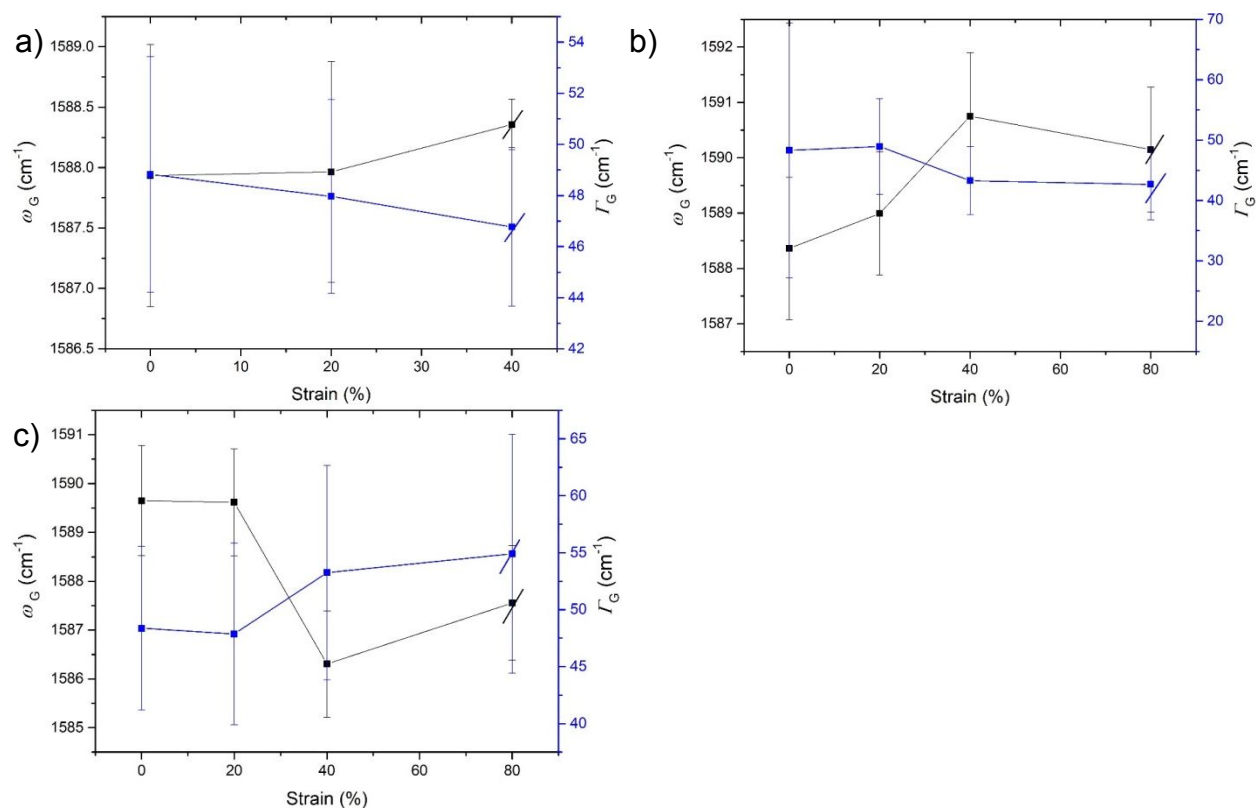


**Figure S19.**  $\omega_G$  and  $I_G$  as a function of strain for (A) p-GO, (B) GO-15, and (C) GO+CNT.

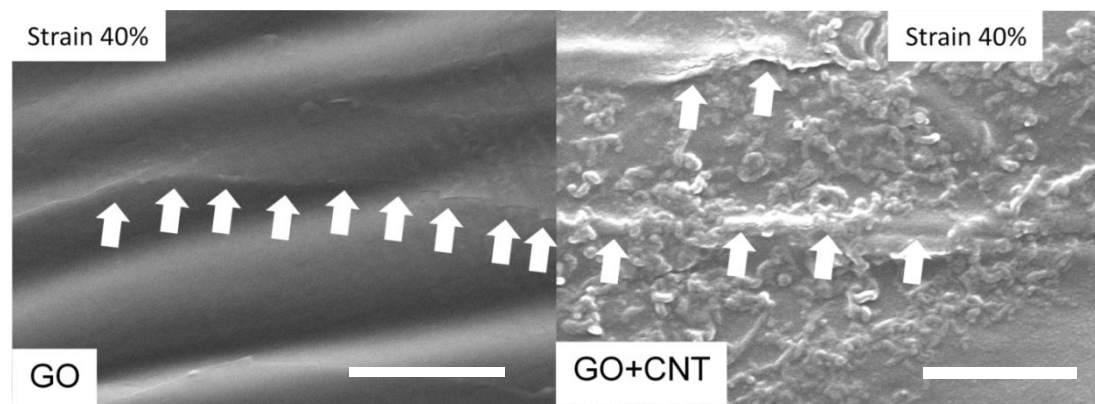


**Figure S20.** SEM images of p-GO and GO+CNT under the strain of 40%. The cracks are arrowed. Scale bar 1  $\mu\text{m}$ .

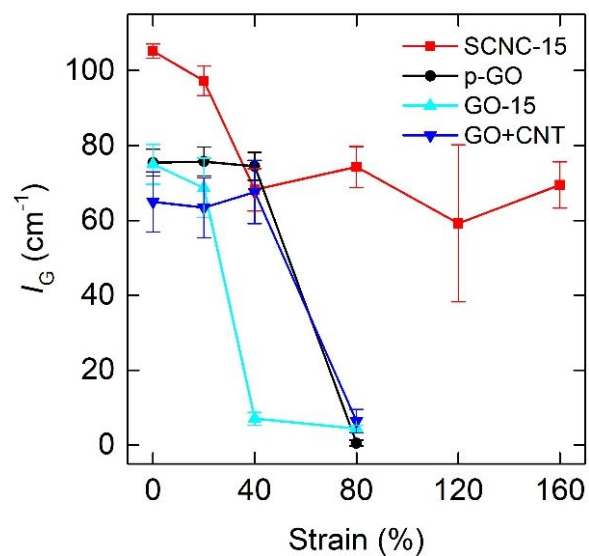


**Figure S21.** Summary of the G mode intensity of samples exposed to different strains. Beyond 120%, the stretch exerted on the carbon bonds of SCNC-15 became limited than intended was applied due to the compressive deformation of the substrate.

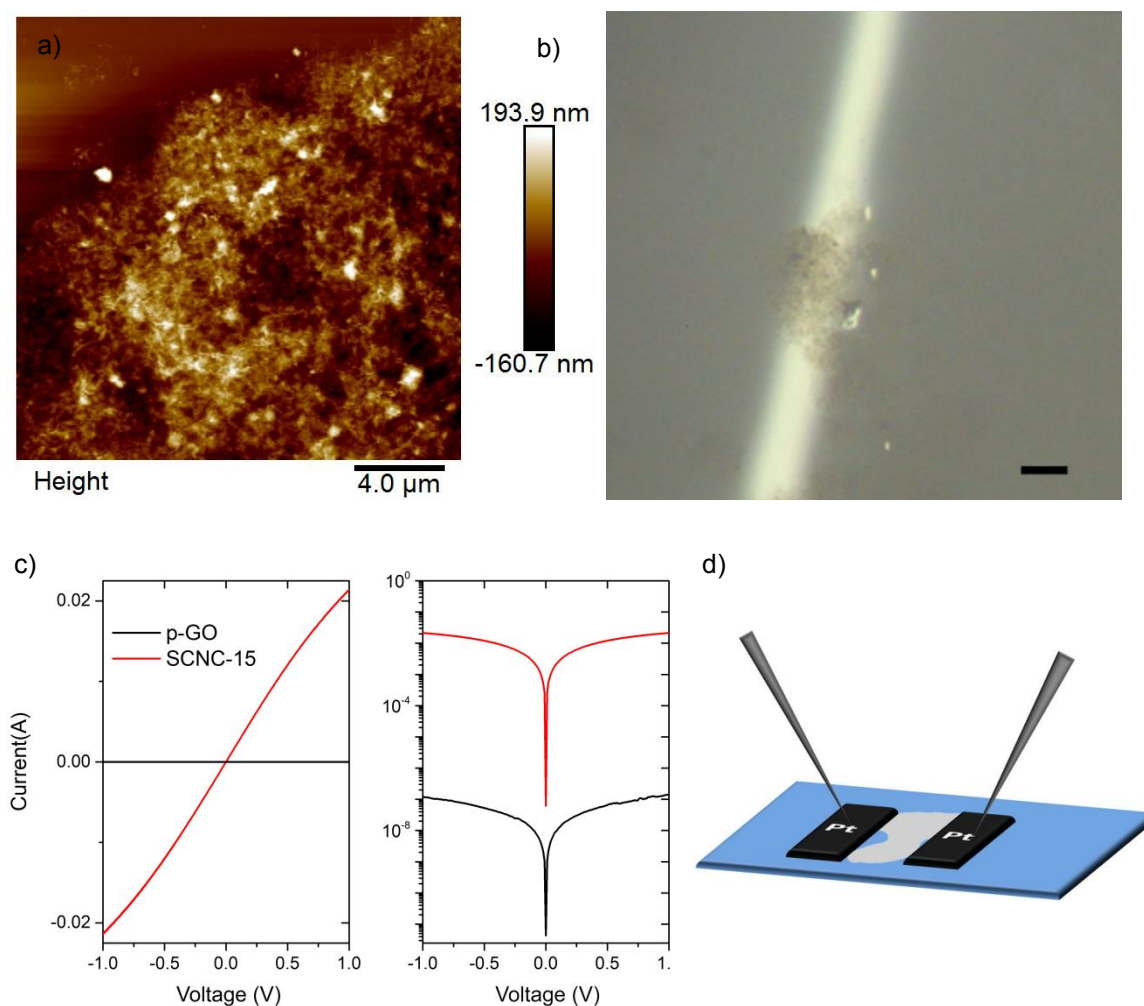


**Figure S22.** a) AFM image of SCNC-15 dried on silicon substrate. b) optical image of SCNC-15 loaded between two electrodes. Scale bar: 20 μm. c) linear and semi-logarithmic I-V curves of p-GO and SCNC-15. d) Illustration of the setup for resistance.

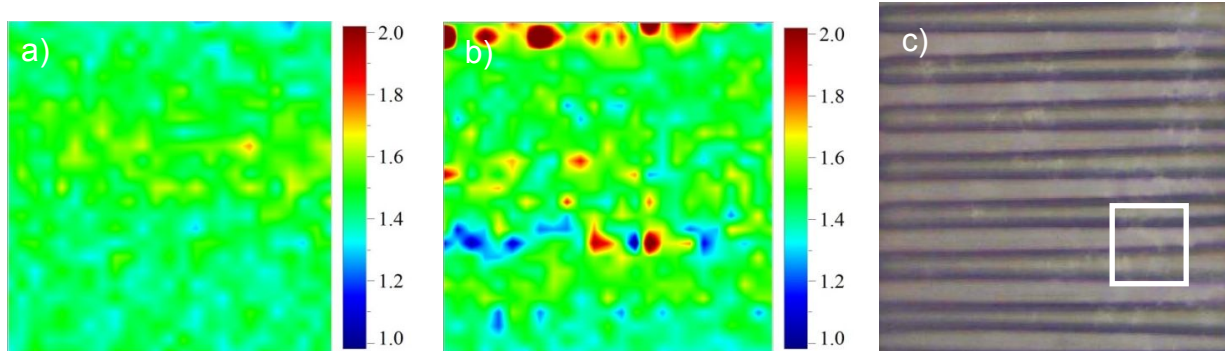


**Figure S23.** Raman map of D/G intensity ratio of SCNC-15 at strain of (a) 0 and (b) 160%. The extremely red area indicates the generation of defective structure. (c) Optical image of the sample at strain of 160% is shown with the white zone detected by RAMAN. Some cracks may happen but most structures of SCNC-15 keep unchanged at the strain of 160%. Scanning area  $25 \times 25 \mu\text{m}^2$ .

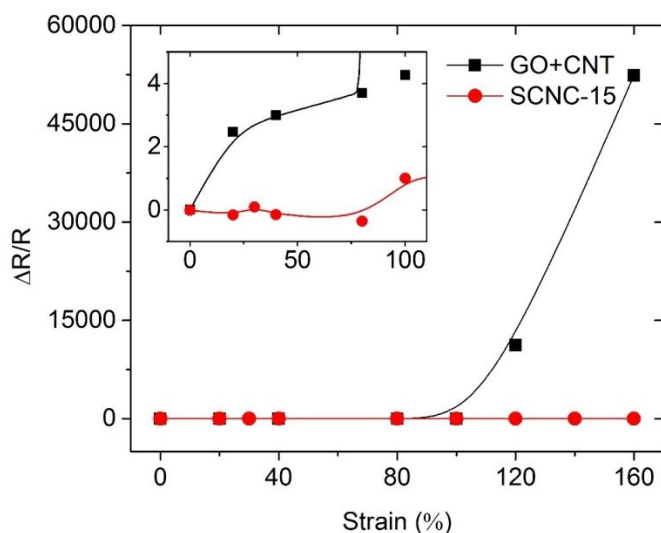


**Figure S24.** Sharp contrast of relative resistance ( $R$ ) change ( $\Delta R/R_0$ , where  $\Delta R = R - R_0$ ,  $R_0$  is the resistance at zero strain) between SCNC-15 and GO+CNT was shown, although they exhibited similar resistance at around zero strain. The inset shows  $R(\text{GO+CNT})$  triples at strain of 40% and increases much more rapidly beyond 80% strain, whereas  $R(\text{SCNC-15})$  only doubles when strain is larger than 100%.

**Table S2.** Reported stretchable nano-carbonaceous materials.

Materials	Reference
Monolayer Gr	Xu, et al, <i>Nat. Commun.</i> <b>2015</b> , 6, 8119.
Bilayer Gr	
Trilayer Gr	
Gr fiber	Cheng, et al, <i>Adv. Mater.</i> <b>2015</b> , 27, 7365–7371.
Suspended Gr ribbon	Huang, et al, <i>Nano Lett.</i> <b>2011</b> , 11, 1241–1246.
Rippled Gr/PDMS	Wang, et al, <i>ACS Nano</i> <b>2011</b> , 5, 3645–3650.
Gr–Nanocellulose/PDMS	Yan, et al, <i>Adv. Mater.</i> <b>2014</b> , 26, 2022–2027.
Gr foam/PDMS	Ha, et al, <i>Adv. Funct. Mater.</i> <b>2015</b> , 25, 4228–4236.
Gr/rubber	Coleman, et al, <i>ACS Nano</i> <b>2014</b> , 8, 8819–8830.
Crumbled Gr/PDMS	Ref 10
Percolative Gr/PET	Hofmann, et al, <i>Nano Lett.</i> <b>2012</b> , 12, 5714–5718.
Gr-CNT/PDMS	Meng, et al, <i>Appl. Phys. Lett.</i> <b>2013</b> , 102, 183511.
Gr sponge /PDMS	Cheng, et al, <i>Nat. Mater.</i> <b>2011</b> , 10, 424–428.
Gr-Gr scroll/PDMS	Ref 12
Aligned CNT/PDMS	Hata, et al, <i>Nat. Nanotechnol.</i> <b>2011</b> , 6, 296–301.
Gr network/PI	Yeo, et al, <i>Adv. Mater.</i> <b>2018</b> , 30, 1704626.
Textured graphene/PDMS	Park, et al, <i>ACS Nano</i> <b>2016</b> , 10, 9446–9455.
Gr foam-CNT/PDMS	Dong, et al, <i>Adv. Mater.</i> <b>2017</b> , 29, 1606411.

## REFERENCE

1. Landau L. D.; Pitaevskii, L. P.; Kosevich, A. M.; Lifshitz, E. M. *Theory of Elasticity*. Elsevier Science, **2012**.
2. Henley, S. J.; Hatton, R. A.; Chen, G. Y.; Gao, C.; Zeng, H.; Kroto, H. W.; Silva, S. R. P. Enhancement of Polymer Luminescence by Excitation-Energy Transfer from Multi-Walled Carbon Nanotubes. *Small* **2007**, *3*, 1927—1933.
3. Hsu, H. C.; Shown, I.; Wei, H. Y.; Chang, Y. C.; Du, H. Y.; Lin, Y. G.; Tseng, C. A.; Wang, C. H.; Chen, L. C.; Lin, Y. C.; Chen, K. H. Graphene Oxide As A Promising Photocatalyst for CO<sub>2</sub> to Methanol Conversion. *Nanoscale* **2013**, *5*, 262—268.
4. Woltornist, S. J.; Oyer, A. J.; Carrillo, J.-M. Y.; Dobrynin, A. V.; Adamson, D. H. Conductive Thin Films of Pristine Graphene by Solvent Interface Trapping. *ACS Nano* **2013**, *7*, 7062—7066.
5. Bagri, A.; Mattevi, C.; Acik, M.; Chabal, Y. J.; Chhowalla, M.; Shenoy, V. B. Structural Evolution During The Reduction of Chemically Derived Graphene Oxide. *Nat. Chem.* **2010**, *2*, 581—587.
6. Chen, C.-M. Surface Chemistry and Macroscopic Assembly of Graphene for Application in Energy Storage. Springer Berlin Heidelberg, Berlin, Heidelberg, 2016; pp 51—71.
7. Liscio, A.; Kouroupis-Agalou, K.; Betriu, X. D.; Kovtun, A.; Treossi, E.; Pugno, N. M.; De Luca, G.; Giorgini, L.; Palermo, V. Evolution of The Size and Shape of 2D Nanosheets During Ultrasonic Fragmentation. *2d Mater.* **2017**, *4*, 025017.
8. Doktycz, S. J.; Suslick, K. S. Interparticle Collisions Driven by Ultrasound. *Science* **1990**, *247*, 1067—1069.